

# Interfacial defect properties of high-entropy carbides: Stacking faults, Shockley partial dislocations, and a new Evans-Polanyi-Semenov relation

Samuel E. Daigle<sup>a</sup>, Stefano Curtarolo<sup>b</sup>, William G. Fahrenholtz<sup>c</sup>, Jon-Paul Maria<sup>d</sup>, Douglas E. Wolfe<sup>e</sup>, Eva Zurek<sup>f</sup>, Donald W. Brenner<sup>a</sup>

<sup>a</sup>Department of Materials Science and Engineering, NC State University, Raleigh, 27695, NC, USA

<sup>b</sup>Thomas Lord Department of Mechanical Engineering and Materials Science, Duke University, Durham, 27708, NC, USA

<sup>c</sup>Missouri University of Science and Technology, Rolla, 65409, MO, USA

<sup>d</sup>Pennsylvania State University, Department of Materials Science and Engineering, State College, 16802, PA, USA

<sup>e</sup>Pennsylvania State University, Applied Research Laboratory, State College, 16802, PA, USA

<sup>f</sup>Department of Chemistry, State University of New York at Buffalo, Buffalo, 14260, NY, USA

## Abstract

Using first principles calculations,  $\{111\}$  intrinsic stacking fault (ISF) energies in Group IVB, VB, and VIB high-entropy transition metal carbides are shown to be predictable from an optimized rule of mixtures based on the properties of the single metal carbide constituents present near the stacking fault. A composition-independent linear relationship is demonstrated between the ISF energies and the unstable stacking fault (USF) energies along the  $\langle 11\bar{2} \rangle \{111\}$  gamma surface slip path. Treating the ISF and USF energies as analogous to the heat of reaction and transition state barrier in chemical reactions, this linear relationship represents a new application of the Evans-Polanyi-Semenov principle. Further, a full defect energy distribution can be obtained from the predicted ISF energies with only the composition as an input for the mixed early-transition metal carbides. Applying a model that balances the elastic repulsion between partial dislocations with the distribution of ISF energies, we show that Shockley partial edge dislocations should remain bound for all valence electron concentration values up to about 9.6, even when the average stacking fault energy is negative.

**Keywords:** Stacking faults, Entropy, Dislocation, Modeling, Carbides

## 1. Background and Motivation

The first high-entropy ceramic, a five cation rocksalt oxide, was reported in 2015 [1]. Since then, the number of high-entropy ceramics has rapidly expanded and now includes a range of different oxides, carbides, diborides, nitrides, carbonitrides, perovskites and other related materials [2–14]. One of the central questions associated with these materials is the degree to which the structural, thermal, mechanical, electronic and chemical properties can be predicted by a rule of mixtures (RoM) based on their constituent compounds, and which properties are unique to a high-entropy ceramic. For example, the rocksalt oxide with cations  $\text{Mg}^{+2}$ ,  $\text{Ni}^{+2}$ ,  $\text{Co}^{+2}$ ,  $\text{Cu}^{+2}$ , and  $\text{Zn}^{+2}$  was found to have a lattice constant that is well described by a RoM and Bader charges that are transferable between the binary, ternary, and high-entropy compositions [15]. However, adding aliovalent cations such as  $\text{Li}^{+1}$  and  $\text{Sr}^{+3}$  results in a range of cation and oxygen charges, multiple valence states, and a reduction in thermal conductivity due to enhanced phonon scattering from the different charge states [16, 17]. For stoichiometric high-entropy carbides with transition metals (HETMCs) from Groups IVB, VB, and VIB, theory predicts that lattice constants, bulk moduli, and cohesive energies are all well described by a RoM from the constitutive rocksalt binaries [18]. The carbon vacancy formation energies, on the other hand, cannot be accurately estimated from a simple RoM, but they can

effectively be estimated using a neural network trained on computational energies [19].

A convenient computational tool to help to understand slip in crystals is the gamma surface. This is generated by moving two adjacent regions of a crystal along a given interfacial plane and calculating the potential energy after relaxing the system in the direction normal to the interface. The potential energy is given as a function of the relative in-plane displacement of the slabs to produce a potential energy landscape equivalent to a topological map. The gamma surface was introduced by Vitek to find energetically stable stacking faults in bcc materials [20], and has since become an invaluable tool for understanding slip and related mechanical deformations. For example, intrinsic stacking fault (ISF) energies (energy valleys) are used to predict partial dislocation separations, while unstable stacking fault (USF) energies (peaks in the gamma surface) can be used to predict energetically favorable slip systems. USF and ISF energies are also used in analytic expressions to predict quantities such as fracture and twinning tendencies. Tadmor and Bernstein, for example, developed an expression for predicting twinning that includes the ratio ISF/USF [21, 22].

For the research reported below, it is important to distinguish between quasi-static shear calculations [23], where energies may include a component of shear stress along the slip plane, and the gamma surface. The former attempts to better

describe the physics of the shear process, while the latter is intended as a convenient tool with features such as the ISF and USF energies that yield insight into mechanical deformation. Hence, stress along a given slip path from a gamma surface is not necessarily a relevant physical quantity with respect to quantities such as dislocation mobility [24].

Experimental and computational studies have established that the rocksalt Group IVB carbides TiC, ZrC, and HfC and the Group VB carbides VC, NbC, and TaC prefer to slip along  $\langle 110 \rangle$  directions [25]. However, the Group IVB carbides slip along  $\{110\}$  planes, while the Group VB carbides slip along  $\{111\}$  planes. Studies of mixed IVB-VB carbides have reported either slip on both planes, or on  $\{111\}$  planes exclusively [26, 27]. By examining the gamma surface with energies calculated from Density Functional Theory (DFT), Thompson, Weinberger and co-workers have shown that the transition from slip on  $\{110\}$  to  $\{111\}$  planes can be attributed to a lowering of the barrier along the  $\langle 112 \rangle \{111\}$  slip direction due to a decrease in the high symmetry ISF energy as composition goes across the columns [25, 28]. Further, slip along the  $[1\bar{1}2]$  direction to the low energy ISF followed by slip along  $[\bar{1}2\bar{1}]$  on  $\{111\}$  planes leads to a net slip along the  $[01\bar{1}]$  direction. The decomposition of  $\langle 110 \rangle \{111\}$  slip is illustrated for fcc Ni by Shang et al. using an alias shear deformation model [29].

Ma et al. have used DFT to calculate the energies along the slip and twinning paths on  $\{111\}$  planes for rocksalt HETMCs containing Zr, Nb, Ta, Hf, Ti, and V [30]. They report that USF energies for the single metal carbides are higher than those for compositions with mixed cations, suggesting that dislocation nucleation would be more prevalent in the latter compared to the binaries. Our calculations described below do not reproduce this result. Instead, we find that the binaries and the high-entropy compositions studied all fall along well-behaved relations regarding ISF and USF energies. In addition, the Ma et al. study did not characterize the shifts in the position of the USF away from the point halfway between the ideal system and the ISF configuration along the slip direction. As shown below, accounting for this shift is critical to accurately calculating the USF energy, and leads to a previously unreported relationship between the ISF and USF.

The intent of the research reported in this paper was to use DFT calculations to explore the degree to which ISF and USF energies along the  $\langle 11\bar{2} \rangle \{111\}$  gamma surface path in stoichiometric Group IVB-VB-VIB HETMCs can be estimated from a RoM from the corresponding values for the single metal rocksalt carbides. The HETMCs compositions in this study are listed in Table 1.

As discussed in more detail below, three general conclusions come from the research. First, based on the DFT results, a RoM with an optimized weighting scheme based on atomic layers near the stacking fault provides energies within  $\pm 0.2$  J/m<sup>2</sup> for both the average and local energies of the ISF. Second, by including Group VIB elements, where rocksalt is not the most energetically stable structure, the average ISF energy of a high-entropy composition can be negative. This is despite these HETMC compositions producing single phase materials, as predicted by entropy descriptors and confirmed by experi-

Table 1: High-entropy carbide compositions studied for each calculation.  $\langle 11\bar{2} \rangle \{111\}$  slip path calculations consisted of 12 simulations at evenly spaced points along the gamma surface. USF calculations were performed at the predicted peak location as presented in Section 3.1. Compositions have been experimentally validated as single-phase [31, 32] except as marked for non-validated (<sup>†</sup>) and multi-phase (<sup>‡</sup>) [32] compositions.

Calculation	Compositions	
ISF	(Cr,Mo,Nb,Ta,W)C	(Cr,Mo,Nb,V,W)C
	(Hf,Mo,Nb,Ta,W)C <sup>†</sup>	(Hf,Mo,Ta,W,Zr)C <sup>‡</sup>
	(Hf,Mo,Ti,W,Zr)C	(Hf,Mo,V,W,Zr)C <sup>‡</sup>
	(Hf,Nb,Ta,Ti,V)C	(Hf,Nb,Ta,Ti,W)C
	(Hf,Nb,Ta,Ti,Zr)C	(Hf,Ta,Ti,W,Zr)C
	(Mo,Nb,Ta,Ti,V)C <sup>†</sup>	(Mo,Nb,Ta,V,W)C
	(Mo,Nb,Ta,W,Zr)C <sup>†</sup>	(Nb,Ta,Ti,V,W)C
$\langle 11\bar{2} \rangle \{111\}$ slip path	(Hf,Nb,Ta,Ti,Zr)C	(Mo,Nb,Ta,V,W)C
USF	(Hf,Nb,Ta,Ti,V)C	(Hf,Nb,Ta,Ti,Zr)C
	(Mo,Nb,Ta,V,W)C	(Nb,Ta,Ti,V,W)C

ment [31]. A random cation arrangement leads to regions of positive and negative energies, which we evaluate statistically. Similar to other work on the effective roughness for slip in high-entropy materials [33–35], it is proposed that these statistical distributions contribute to the Peierls stress through a “mean+1” model discussed below that prevents partial dislocations from separating into extended stacking faults. Finally, it was found that the USF position is not always at the high-symmetry point halfway between the ideal system and the ISF, but rather can exist earlier or later along the slip path. This peak shift is apparent from literature gamma surfaces for transition metal carbides, such as those presented by Yu et al. [25], but has not previously been quantified. We find that the peak shift can be defined as a monotonic function of the ISF. When the correct peak position is used, there is a linear relationship between the USF and the ISF energies that spans both net negative and net positive ISF values.

As a result of these relationships, the ISF energy can be found via a RoM, while the associated USF and the peak shift can be estimated from monotonic functions. The linear relation between the USF and ISF is analogous to the well-established Evans-Polanyi-Semenov (EPS) relation [36], where for a class of similar chemical reactions, the energy barrier is linearly proportional to the heat of reaction.

## 2. Calculation Details

The energies were calculated from DFT using the plane-wave projector-augmented-wave pseudopotential methods [37] in the Vienna Ab initio Simulation Package [38–40]. The exchange-correlation potential used was the Perdew et al. [41] parameterization of the generalized gradient approximation. The plane-wave basis cutoff energy was 520 eV with a  $6 \times 6 \times 1$   $\Gamma$ -centered k-point mesh. Spin polarization was enabled for all simulations to account for possible magnetism in the group VIB transition metals.

Gamma surface configurations for the rocksalt carbides were constructed as translations of an 80-atom slab with two (111) free surfaces separated by at least 12 Å of vacuum. The x and y supercell vectors were defined as the  $\frac{1}{2}[11\bar{2}]$  and  $[\bar{1}10]$  directions, respectively. For each composition, 50 random arrangements of the cation sites were generated. Relaxations were performed with respect to the atomic positions in the [111] direction, while keeping the supercell dimensions fixed along with the x and y coordinates. Lattice parameters for the high-entropy carbide compositions were determined by the average result of energy minimization performed on 10 randomly arranged 80-atom bulk rocksalt structures with supercell vectors of [210],  $[\bar{1}20]$ , and [002].

All calculations in these studies were performed with full carbon stoichiometry. Transition metal carbides are often carbon deficient, especially at elevated temperatures, and carbon vacancies can affect stacking fault energies [42]. However, vacancy effects in small supercells require additional considerations and are not captured in this work.

Gamma surface energies  $\gamma$  were calculated for each configuration and the constituent binaries using the expression

$$\gamma = \frac{E_\gamma - E_{slab}}{A} \quad (1)$$

where  $E_\gamma$  and  $E_{slab}$  are the energy of the translated and vacuum slab configurations, respectively, and  $A$  is the cross-sectional area of the supercell in the (111) plane. The local environment of any point on the (111) gamma surface can be defined by the translation vector between the upper and lower portions of the slab and the local atomic environment in the nearby (111) cation planes.

### 3. Results and Discussion

The compositions in Table 1 were studied to determine the relationship between ISF energy, USF energy, and the USF position along the  $\langle 11\bar{2} \rangle \{111\}$  slip path. Because the shape of the gamma surface varies with composition at the stacking fault, a larger set of calculations was required to find the USF peak position for a given configuration. Compositions were divided into three separate simulation regimes to efficiently characterize the critical points of the slip path.

#### 3.1. Stacking Fault Energies

Stacking faults in high-entropy compounds differ from those of single-component materials in that the energy is dependent on the arrangement of nearby atoms in the structure. Similar to vacancies in high-entropy alloys and ceramics, the defect energy can be defined as a distribution of energies based on the local atomic environment [18, 19, 43], in this case defined as the composition along the interface. The energy dependence on the local arrangement of atoms requires a sample of different atomic configurations from each tested composition. The sample can then be used to fit a model and predict the total energy distribution across the configurational space, enabling analysis of the impact of defects on bulk properties and phenomena [43].

Table 2: Binary carbide stacking fault energies  $\gamma^{isf}$  in J/m<sup>2</sup> for the single metal rocksalt carbides used in Eq. 2.

	IVB		VB		VIB
Ti	2.757	V	0.453	Cr	-0.777
Zr	2.645	Nb	0.667	Mo	-1.002
Hf	2.691	Ta	0.572	W	-1.353

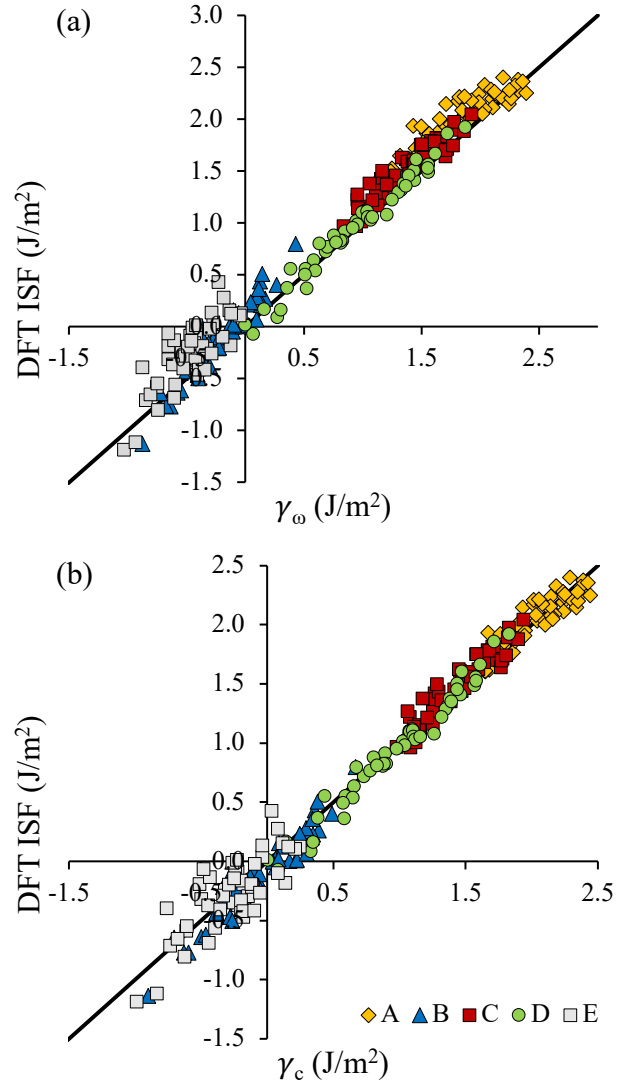


Figure 1: DFT calculated ISF energies as a function of RoM values using layer-dependent weighting for five compositions A:(Hf,Nb,Ta,Ti,Zr)C, B:(Mo,Nb,Ta,V,W)C, C:(Hf,Nb,Ta,Ti,V)C, D:(Hf,Nb,Ta,Ti,W)C, and E:(Cr,Mo,Nb,V,W)C. RoM fit from (a) layer weights only using Eq. 2 and (b) corrected RoM using Eq. 3.

Here, DFT energies were calculated for 50 random ISF configurations of 14 HEC compositions (see Table 1).

ISF energies in HETMCs can be approximated by a weighted RoM of the single metal carbide stacking fault energies for atoms within 0.5 nm of the defect plane as

$$\gamma_\omega^{isf} = \sum_i \sum_k \frac{\omega_k n_{ik} \gamma_i^{isf}}{n_k}. \quad (2)$$

Here,  $n_{ik}$  are the number of atoms of each alloying element  $i$  in each layer  $k$ ,  $\gamma_i^{isf}$  are the  $\{111\}$  stacking fault energies in the binaries, and  $\omega_k$  are the fitted layer weights. For the 80 atom supercells in this work,  $n_k = 4$ , and the normalized weights  $\omega_{1-4}$  are found to be 0.589, 0.321, 0.045, and 0.045, respectively. While the layer weights are calculated as fitted parameters, they decrease with increasing distance from the defect, corresponding with a qualitative decay function representing some unknown physical interaction. The energies of the single metal carbide stacking faults are given in Table 2.

Here we note that the ISF energies for group VIB metal carbides are all negative, as these compositions prefer the hexagonal WC or Mo<sub>2</sub>C structure (P6m2) to the rocksalt structure (Fm3m). In HETMCs, these elements can be present as equimolar components [31, 32], resulting in negative stacking faults for certain stacking fault configurations within the stable structure. The consequences of negative stacking faults in HETMCs are considered in Section 3.3.

Using the single metal carbide stacking fault energies in Table 2 and the given weights  $\omega$ , the optimized RoM gives a reasonable approximation of the high-entropy ISF energies, as plotted for five compositions in Fig. 1a. However, comparing the RoM prediction to the DFT data in Fig. 1, it is apparent that compositions with high and low ISF energies are underestimated by a RoM and that the distribution of energies within each composition is itself biased. This bias is accounted for by fitting two separate quadratic functions, first to the bulk RoM ISF energies  $\bar{\gamma}$  for each composition and second to the local weighted RoM  $\gamma_\omega$  as expressed in Eq. 2. The results are plotted for the same five compositions in Fig. 1b. These empirical corrections reduce the root mean squared error by 26% from 182 mJ/m<sup>2</sup> to 135 mJ/m<sup>2</sup>. The error for high [(Hf,Nb,Ta,Ti,Zr)C] and low [(Cr,Mo,Nb,V,W)C] valence electron concentration (VEC) compositions are reduced by 55% and 27% respectively. The fitted model is given as

$$\gamma_c^{isf} = (0.456\bar{\gamma} - 0.335)^2 - (0.303\gamma_\omega - 1.835)^2 + 3.393, \quad (3)$$

with model errors for each composition presented in Table 3. In all cases, the ISF energies for stacking fault configurations in HETMCs are well described as an average of the binary single metal carbide constituents near the interface.

The USF energy is another useful tool for understanding dislocation slip in fcc materials. However, because it is not necessarily at a high symmetry position, it can be expensive to calculate in DFT compared to the ISF. This is illustrated by the energies along the  $\frac{1}{6}\langle 11\bar{2} \rangle \{111\}$  slip path for two high-entropy compositions and four arrangements per composition plotted in Fig. 2.

While the intrinsic stacking fault is always at the high symmetry position, the USF can vary significantly from the center of the slip path between compositions, and between arrangements within the same composition. The traditional approach is to scan the gamma surface with a grid along the dislocation vector. Because the location of the USF peak is not fixed along this vector, it is often required to use a fine grid to calculate

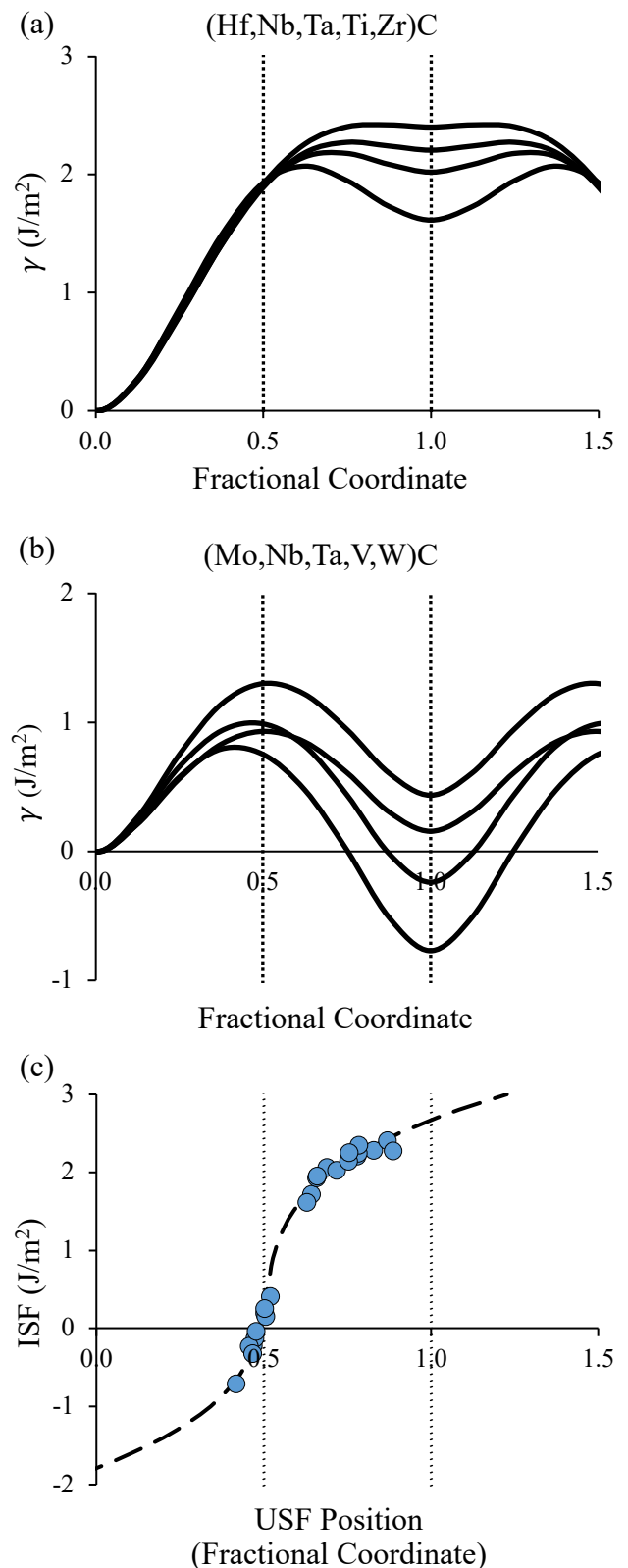


Figure 2: Calculated gamma surface energies along the  $\frac{1}{6}\langle 11\bar{2} \rangle \{111\}$  slip direction for four atomic configurations of (a) (Hf,Nb,Ta,Ti,Zr)C and (b) (Mo,Nb,Ta,V,W)C. ISF and midpoint are indicated by the dashed vertical lines, while (c) shows the relationship between ISF and the interpolated peak position and a fitted third order polynomial for initial N-R estimate.

Table 3: Root mean squared fitting errors for the weighted RoM stacking fault models  $\gamma_{\omega}^{isf}$  and  $\gamma_c^{isf}$  (J/m<sup>2</sup>).

Composition	RMSE ( $\gamma_{\omega}^{isf}$ )	RMSE ( $\gamma_c^{isf}$ )
(Cr,Mo,Nb,Ta,W)C	0.294	0.220
(Cr,Mo,Nb,V,W)C	0.263	0.192
(Hf,Mo,Nb,Ta,W)C	0.164	0.121
(Hf,Mo,Ta,W,Zr)C	0.163	0.135
(Hf,Mo,Ti,W,Zr)C	0.111	0.124
(Hf,Mo,V,W,Zr)C	0.146	0.126
(Hf,Nb,Ta,Ti,V)C	0.171	0.103
(Hf,Nb,Ta,Ti,W)C	0.082	0.088
(Hf,Nb,Ta,Ti,Zr)C	0.227	0.102
(Hf,Ta,Ti,W,Zr)C	0.145	0.117
(Mo,Nb,Ta,Ti,V)C	0.146	0.151
(Mo,Nb,Ta,V,W)C	0.163	0.123
(Mo,Nb,Ta,W,Zr)C	0.170	0.113
(Nb,Ta,Ti,V,W)C	0.137	0.136

an accurate maximum value for the energy barrier. This is especially expensive for high-entropy materials, where multiple configurations are necessary.

Here, an estimate of the USF peak location is combined with a Newton-Raphson (N-R) root-finding algorithm to predict the coordinates of the barrier on the gamma surface and minimize computation time required to simulate the relevant configurations. For the N-R method, the root of a differentiable function can be found with increasing accuracy by calculating the x-intercept of the tangent line at an initial guess and iterating until sufficient accuracy has been obtained. In the case of the USF, we must consider the second derivative of the gamma surface to locate the local maximum of the function.

Using a coarse grid for several random configurations of two compositions (Hf,Nb,Ta,Ti,Zr)C and (Mo,Nb,Ta,V,W)C representing the range of ISF energies for the HETMCs, the shape of the gamma surface can be characterized along the  $\langle 11\bar{2} \rangle$  vector to identify the critical points (Fig. 2). The USF is near the high symmetry position at  $\frac{1}{12}[11\bar{2}]$  for (Mo,Nb,Ta,V,W)C, but is shifted toward the ISF for (Hf,Nb,Ta,Ti,Zr)C. From these two compositions, a preliminary function for peak shift is obtained as a third order polynomial with respect to the ISF and used to initiate the N-R search. Starting from this function, plotted in Fig. 2c, the DFT energy at the predicted peak and at one point on either side are used to find the finite differences second derivative. Extrapolating this slope to the x-intercept gives the improved estimate for the USF peak location, where the final DFT energy can be calculated. Given knowledge of the shape of the gamma surface, the first N-R iteration is sufficient despite beginning from an arbitrarily chosen polynomial fit.

Plotted in Fig. 3 are the USF energies calculated for the  $\langle 11\bar{2} \rangle\{111\}$  gamma surface as a function of ISF energy. For the data plotted in Fig. 3a, the USF energy is calculated at the midpoint along the slip direction ( $\frac{1}{12}[11\bar{2}]$ ), while the USF energy plotted in Fig. 3b is the maximum along the entire slip path. There are clear linear relations in both that are discussed in the following section in terms of the EPS principle.

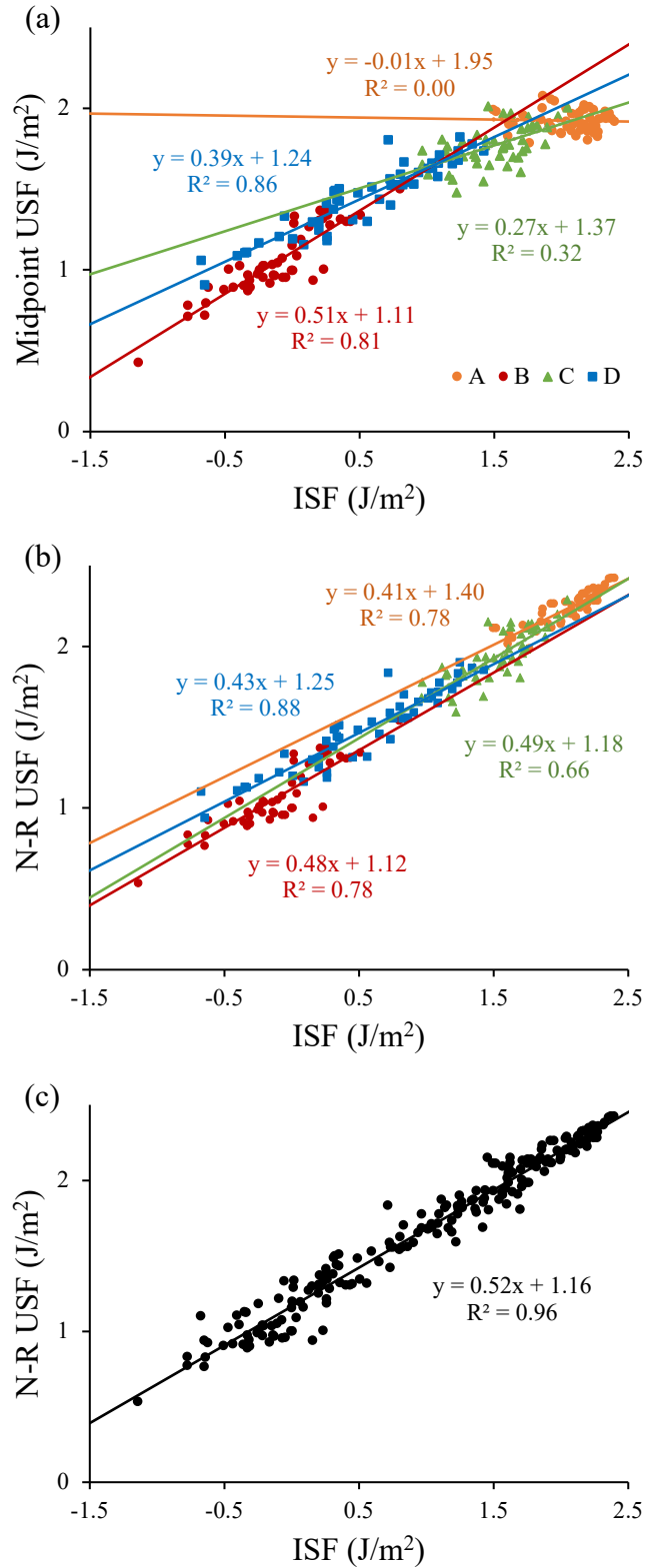


Figure 3: USF energy plotted as a function of the ISF energy at (a) the midpoint along the slip direction, (b) and (c) at the maximum along the path as estimated by N-R. (a) and (b) are broken down by composition. A: (Hf,Nb,Ta,Ti,Zr)C, B: (Mo,Nb,Ta,V,W)C, C: (Hf,Nb,Ta,Ti,V)C, D: (Nb,Ta,Ti,V,W)C. Lines are linear fits to the data.

### 3.2. Evans-Polanyi-Semenov Relations

The EPS relation (also referred to as the Bell–Evans–Polanyi or Brønsted–Evans–Polanyi principle) states that for a given set of related chemical reactions, the activation energy  $E_A$  for a chemical process is proportional to the heat of reaction  $\Delta H$  as

$$E_A = E_A^0 + \alpha\Delta H \quad (4)$$

where  $E_A^0$  and  $\alpha$  are constants [36]. This simple relation has impacted multiple areas of chemistry, including combustion [44], organic synthesis [45, 46], photo-chemistry [47, 48], polymerization [49], interstellar chemistry [50], heterogeneous catalysis [51–54], gel degradation [55], surface diffusion [56], energetic materials sensitivity [57–59], materials discovery [60], and fundamental chemical kinetics [61–63]. Adding to this body of work, we propose the ISF and USF energies as an analogous set of quantities to the heat of reaction and activation energy, respectively.

One central premise of HETMCs has been that their properties are continuously tunable by a RoM through the IVB-VIB elements, for example as discussed in Section 3.1 in the context of stacking faults. VEC is another quantity calculated as a RoM from constituent elements, used both as a theoretical construct within the electronic band structure [64] and as a way of accounting for composition, including cations as well as carbon and nitrogen fraction [65]. In the context of the EPS relation, it is relevant to explore (1) whether the EPS relation is maintained for the continuous range of ISF and USF values on a gamma surface, and if so (2) whether the  $E_A^0$  and  $\alpha$  values are constant or composition dependent.

The data plotted in Fig. 3a, where the USF energies are calculated at the high symmetry position, is grouped by composition with a separate linear fit for each. For compositions A and B, the  $R^2$  values indicate that the data is relatively well described by an EPS relation, but with different intercepts and slopes ( $E_A^0$  and  $\alpha$  values). The linear fit for composition C is less accurate (smaller  $R^2$  value), while there appears to be little correlation for composition D. Hence, if using the midpoint energy, the EPS relation seems to be composition dependent. However, when using the maximum energy along the slip path for the USF (Fig. 3b), all four data sets show a linear correlation and similar slopes and intercepts. Plotted in Fig. 3c is the data combined for all compositions, again using the maximum energy along the slip path. It is clear that an EPS relation exists between the ISF and USF energies, and that this relation holds across compositions when the accurate USF energy is used.

Plotted in Fig. 4 are deviations of the USF position from the center point along the  $\langle 11\bar{2} \rangle \{111\}$  gamma surface for the data in Fig. 3c. There is a monotonic, continuous relationship between the position of the USF (the transition state) and the ISF energy (the reaction product). The larger the ISF, the later the USF occurs along the slip direction.

Along with the data for ISF as a function of USF peak shift in Fig. 4, the error function

$$I(x) = B \operatorname{erf}(ax) + \Delta \quad (5)$$

is plotted along the entire length of the slip path using fitting parameters  $B = 2.245 \text{ J/m}^2$ ,  $a = 4.605$ , and  $\Delta = 0.559 \text{ J/m}^2$ .

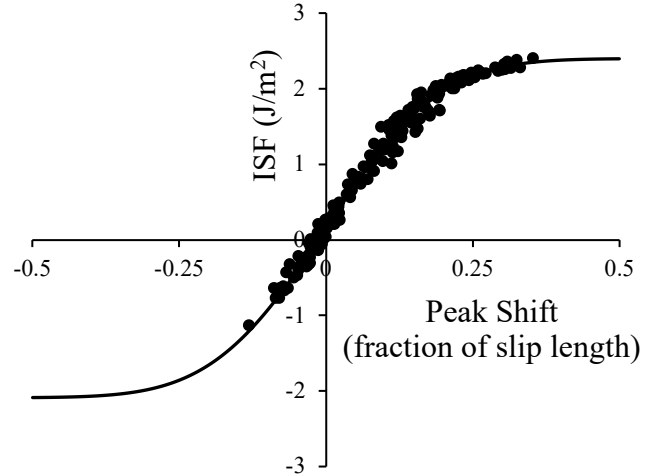


Figure 4: USF peak shift from Newton-Raphson search along  $\langle 11\bar{2} \rangle \{111\}$  gamma surface. Fitting function obtained from Eq. 5 using data from the four compositions specified in Table 1.

Although the physical interpretation of an error function is unclear, it provides a good quantitative fit to the data (a logistic function provides a similar fit). In particular, the asymptotic behavior of the error function is consistent with the range of possible positions of the USF along the slip path, existing only on the region between the ideal structure and the ISF.

This function enables the evaluation of critical points on the gamma surface while minimizing the number of necessary calculations along the slip path. Given an ISF energy, which is well approximated by a weighted RoM, one can identify the position of the USF and perform a single DFT calculation without the need for an iterative search algorithm along the slip path.

The relationships in Fig. 3 and Fig. 4 can be understood using an energy curve overlap model [36, 66], illustrated in Fig. 5. In this model there are two curves that correspond to local energy minima on the gamma surface along the  $[11\bar{2}]$  sliding direction. One curve has a minimum at the ideal structure, while the other has a minimum at the ISF, shifted uniformly in energy according to the ISF energy. The energy along the entire path within this model is the minimum of the two curves at any given point. Fig. 5 illustrates the model for the three cases of  $\text{ISF} > 0$ ,  $\text{ISF} = 0$ , and  $\text{ISF} < 0$ , with the barrier corresponding to the energy where the two curves intersect (the maximum in the solid curve). In the case of  $\text{ISF} > 0$ , the position of the barrier along the sliding path is later than the center position. Consistent with the simulation data, as the ISF energy decreases the value and position of the USF decreases along the slip direction.

The energy curves in Fig. 6 are a two-parameter fit assuming Gaussian functions of the form

$$E(x) = \frac{A}{\sigma\sqrt{2\pi}} \left[ 1 - \exp\left[-\frac{1}{2}\left(\frac{x-x_0}{\sigma}\right)^2\right] \right] \quad (6)$$

for the two overlapping energy curves. Here  $x_0 = 0$  for the curve starting at the ideal structure,  $x_0 = 1$  for the curve starting at the ISF,  $\sigma = 0.7$  and  $A = 9.15 \text{ J/m}^2$ . The simple model is able to qualitatively describe both the relations between USF

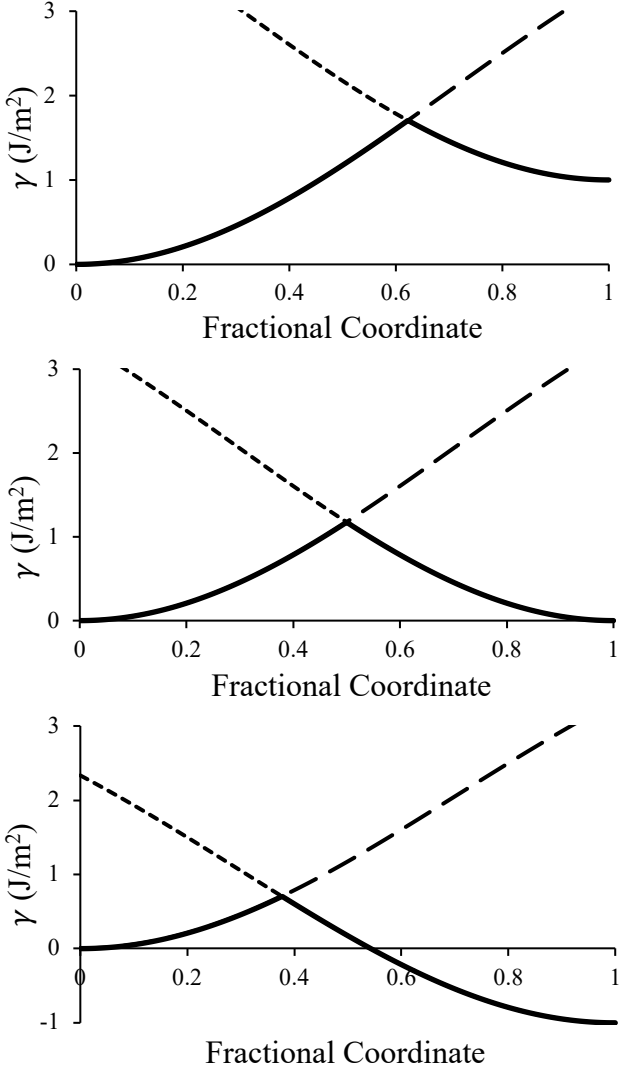


Figure 5: Shifted energy curve model using Eq. 6 plotted along the  $\frac{1}{6}\langle 11\bar{2}\rangle\{111\}$  slip direction for (top) positive, (middle) zero, and (bottom) negative ISF.

and ISF, and between ISF and the shift in USF position along the  $[11\bar{2}]$  direction.

Similar fits to the data can be achieved with other potential energy approximations such as quadratic energy wells, sine fitting, or a Lennard-Jones potential. None of the approximations tested, however, have a clear physical interpretation or other advantages over the two-parameter Gaussian fit.

### 3.3. Shockley Partial Dislocation Separations

Pairs of Shockley partial dislocations in an fcc crystal are connected by a stacking fault such that the equilibrium distance between partials is determined by a balance of the elastic repulsion and the stacking fault energy. One of the interesting issues in high-entropy materials is that they can have negative stacking fault energies while still being phase stable [35, 67]. In non-random crystals, negative stacking fault energies suggest that any Shockley partial dislocations that form should move as far apart as possible, because both the elastic repulsion and the

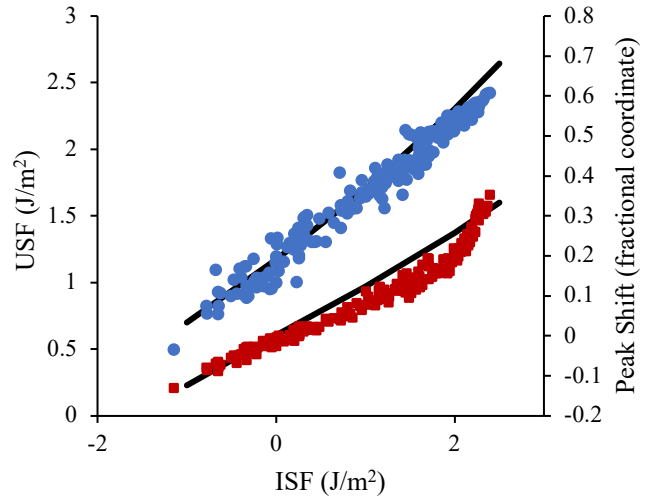


Figure 6: Maximum USF energies (blue circles) and deviations from the center point along the  $\langle 11\bar{2}\rangle\{111\}$  gamma surface where these energies are found (red squares) for data plotted in Fig. 3. The solid lines are two parameter fits for an energy curve overlap model using Eq. 6.

stacking fault formation energy would favor infinite distances. However, large numbers of stacking faults are not always observed experimentally. As an example in a HETMC, the simulations in Section 3.1 indicate that  $(\text{Mo,Nb,Ta,V,W})\text{C}$  has an average stacking fault energy of  $-0.09 \text{ J/m}^2$  such that the elastic repulsion between any Shockley partials should create a significant stacking fault area. Experimentally, however, this composition exhibits sharp x-ray diffraction peaks that suggest a low defect density [32].

One suggestion to account for the apparent lack of stacking faults associated with Shockley partials is that “roughness” from the atomic disorder in high-entropy materials inhibits the ability of the partials to fully separate [33, 34]. While the relation between Peierls stress and stacking fault energy is unclear [67], it is reasonable to assume that this roughness is qualitatively related to the variations in stacking fault energies from a random composition along the interface as the partial dislocations attempt to separate.

This concept is illustrated in Fig. 7, which shows a schematic of two Shockley partial edge dislocations separated by a stacking fault along the blue plane. The peaks on the energy landscape represent a measure of the stacking fault energy contributions to the Peierls stress. A negative stacking fault energy should lower the Peierls stress, while a positive stacking fault energy (denoted by the orange peaks) should increase the Peierls stress. Because the extra half plane exists along the length of an edge dislocation, the positive regions will pin the plane at different points despite the negative stacking fault regions exhibiting a lower local Peierls barrier. Taken to an extreme, even when the net stacking fault energy is negative, positive regions would prevent the Shockley dislocations from moving.

In a set of atomic simulations by Shih et al. [35] that modeled random NiCo alloys with dissociated Shockley partial edge dis-

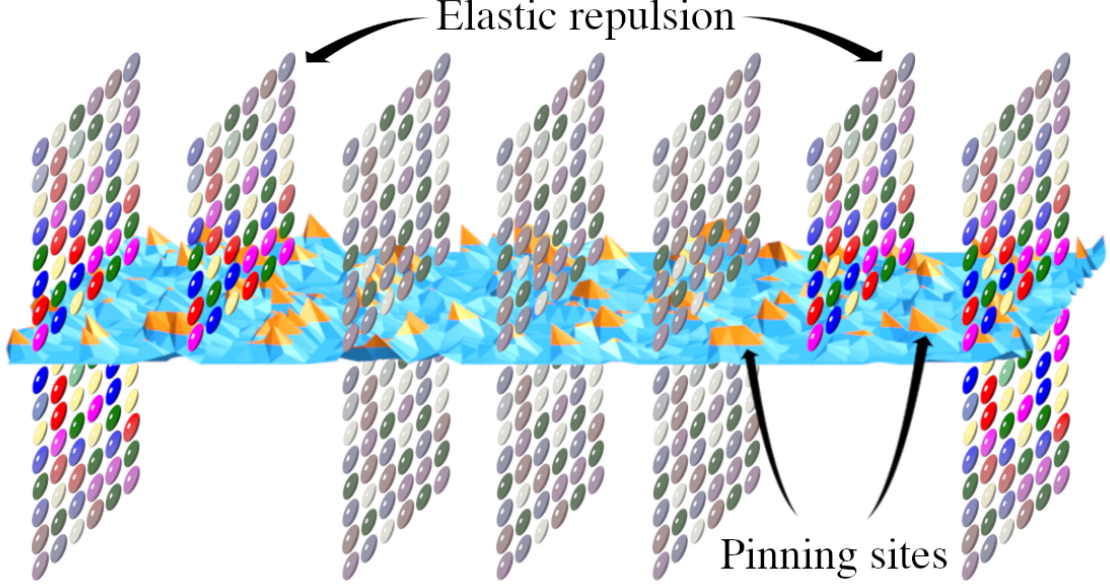


Figure 7: Depiction of two Shockley partial dislocations separated by a stacking fault along the horizontal plane. Brightly colored atoms at the edge dislocations correspond to the local atomic environment that contributes to the Peierls stress, with blue regions representing negative stacking fault regions and orange peaks on the energy landscape representing the high energy pinning sites preventing partial dislocation separation.

locations, the partials remained at finite separations that were less than the distance at which the mean plus one standard deviation ( $\mu + \sigma$ ) of the stacking fault energy distribution equaled the repulsive elastic stress. For this mean + 1 model, we generalize the trend for partial edge dislocation separation length  $s$  with the expression

$$s < \frac{Gb^2}{2\pi(\mu + \sigma)} \quad (7)$$

where  $G$  is the shear modulus,  $b$  is the Burger's vector, and  $\mu + \sigma$  is again the sum of mean and standard deviation of the stacking fault energy distribution.

Sampling from a random distribution of interface cation arrangements, a predicted distribution of ISF energies can be generated for each composition. Critically, the distribution is dependent on the volume that is considered to be part of the local environment. Taken to both extremes for the five cation system, the distribution of energies for a single-atom volume will consist of five peaks corresponding to the five constituent elements, each accounting for 20% of the total distribution. Similarly, as the volume of the local environment increases to infinity, the distribution will approach the delta function centered on the distribution mean.

The volume of the local area can be defined by sampling for each element from a gamma distribution such that

$$X_i \sim \Gamma(\alpha = \frac{n}{N}, \beta = 1) \quad (8)$$

where  $\alpha$  and  $\beta$  are the  $\Gamma$  shape and rate parameters,  $n$  is the number of atoms in the local environment,  $N$  is the number of distinct elements on the lattice site.

In this work, the depth of the local environment was determined from the fitting in Section 3.1. Sampling each (111)

plane separately, the distribution of interface cation arrangements is built from  $X_i \sim \Gamma(1, 1)$ , equating to a naive assumption of  $n = N$ . Without knowing the shape or size of the critical area, this assumption corresponds with a cutoff distance on the order of  $2b$ .

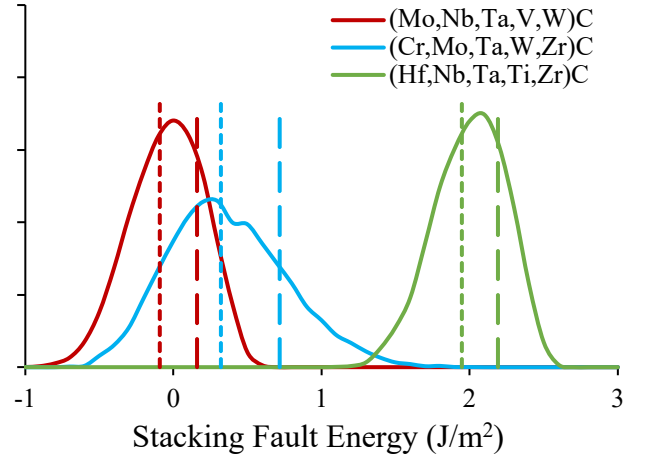


Figure 8: ISF distributions for three compositions. The dashed vertical lines represent the mean and the mean plus one standard deviation for each distribution.

The predicted ISF distributions derived from this  $\Gamma$  sampling and the modified RoM model in Section 3.1 are plotted in Fig. 8 for three different compositions. The mean and mean plus one standard deviation for each distribution are indicated by the dashed vertical lines. For the (Mo,Nb,Ta,V,W)C composition, the mean stacking fault energy and standard deviation are  $-0.09 \text{ J/m}^2$  and  $0.25 \text{ J/m}^2$ , respectively. Using  $G = 193 \text{ GPa}$  and  $b = 0.437 \text{ nm}$  [68] in Eq. 7 yields a Shockley partial separa-



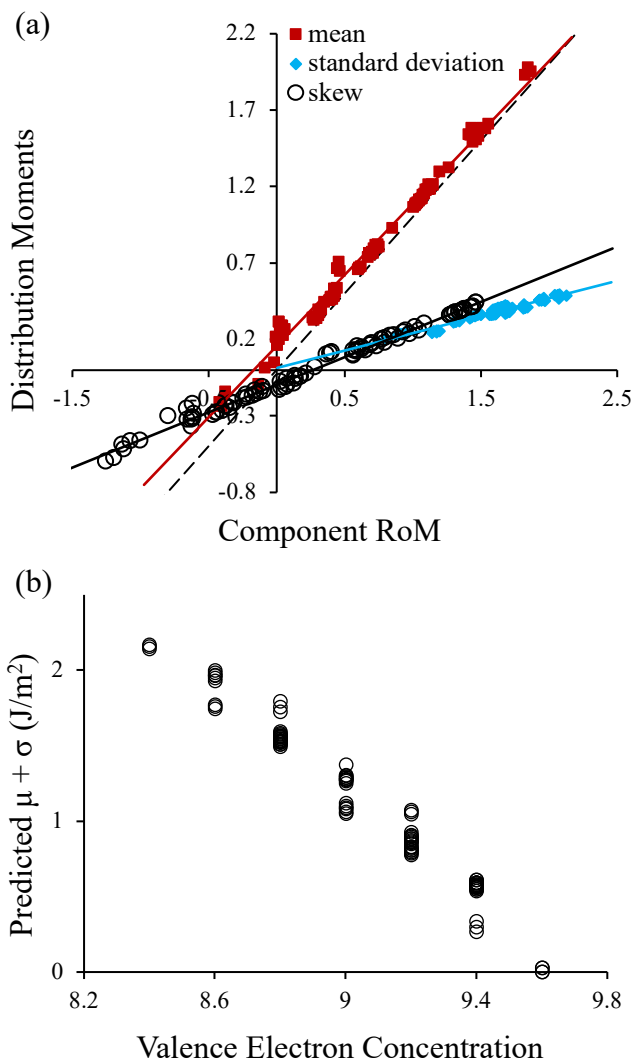


Figure 9: For 94 HETMC compositions, (a) mean, standard deviation, and skew of the predicted ISF energy distributions as a function of the same quantities calculated from the five corresponding single-metal carbide constituents and (b) the sum of first two moments as a function of VEC.

tion  $s$  of less than 18 nm. Hence, although 64% of the stacking fault distribution is negative, the model predicts a finite partial separation.

Plotted in Fig. 9 are the mean, standard deviation and skew of the stacking fault energy distributions for each HETMC composition calculated from a random sample of configurations as a function of the same quantities calculated from just the five constituent single metal carbide ISFs. There are strong linear relations such that the first three moments of the full ISF distributions for a given composition can be estimated from only the binaries, adding another facet to the RoM. The linear coefficients are given in Table 4.

The mean + 1 stacking fault energies, as calculated from the predicted distribution moments, are plotted as a function of their VEC in Fig. 9b for 94 HETMC compositions consisting of five cation combinations from Cr, Hf, Mo, Nb, Ta, Ti, V, W, and Zr. There is a monotonic decrease in energy, suggest-

	$\alpha$	$\beta$	RMSE
Mean	0.932	0.156	0.058
Standard deviation	0.228	0.015	0.015
Skew	0.361	0.096	0.026

Table 4: Linear coefficients  $\alpha$  (slope) and  $\beta$  (intercept) for the first three moments of the predicted ISF distribution along with fitting error (J/m<sup>2</sup>) for 94 HETMC compositions in Fig. 9.

ing that the separation between Shockley partial dislocations increases with increasing VEC. However, because the mean + 1 model estimates a lower bound, partial dislocation separation distances are expected to be finite for all VEC values  $\leq 9.6$ .

#### 4. Conclusion

First principles calculations were used to establish new RoMs for interfacial defects in group IVB, VB, and VIB stoichiometric transition metal carbides. Energies of {111} ISFs were shown to be predictable from an optimized RoM based on values from the respective single metal carbide compositions. A linear relationship was discovered between these stacking fault energies and the USF energies along the  $\langle 11\bar{2} \rangle \{111\}$  slip path on the gamma surface. Provided that the positional shift of the USF from the high symmetry position is accounted for, the linear coefficient is independent of composition. The ISF and USF energies are analogous to the heat of reaction and transition state barrier in chemical reactions, and this linear relationship is similarly analogous to the EPS relationship that is ubiquitous across chemical systems, but not applied to plasticity in solids.

It was further found that the mean, standard deviation, and skew for the distribution of stacking fault energies that result from disorder of cations around the boundary are predictable from linear relations that connect the stacking fault energies of the binaries to the corresponding high-entropy compositions. Using a model where the upper tail of the ISF distribution balances the elastic repulsion between partial dislocations, we demonstrate why Shockley partial edge dislocations remain bound for HETMC compositions with  $VEC \leq 9.6$  despite certain compositions exhibiting negative mean ISF energies. The mean plus one standard deviation is proposed as an upper bound for determining the partial separation. This is consistent with experiment, where compositions predicted to have negative stacking fault energies such as (Mo,Nb,Ta,V,W)C are phase stable with relatively low defect densities [32].

The RoMs and linear relations discovered in this study are important for understanding and predicting the defect structure and mechanical properties of HETMCs. In addition, the EPS relation has been an invaluable tool for estimating reaction kinetics across diverse areas of chemistry, and based on our results we anticipate that it will find other applications in predicting mechanical properties of high-entropy materials. Future work on this topic should include vacancy effects on gamma surface energies, and may require more sophisticated machine learning techniques for quantitative predictability [19, 69].

## 5. Acknowledgments

We would like to gratefully acknowledge the DoD SPICES MURI sponsored by the Office of Naval Research (Naval Research contract N00014-21-1-2515) and for their financial support of this work, as well as the Office of Naval Research for funding through grant N00014-23-1-2758. We also acknowledge the computing resources provided by North Carolina State University High Performance Computing Services Core Facility (RRID:SCR.022168).

## References

- [1] C. M. Rost, E. Sachet, T. Borman, A. Moballegh, E. C. Dickey, D. Hou, J. L. Jones, S. Curtarolo, J.-P. Maria, Entropy-stabilized oxides, *Nat. Commun.* 6 (1) (2015) 8485. doi:10.1038/ncomms9485.
- [2] C. Oses, C. Toher, S. Curtarolo, High-entropy ceramics, *Nat. Rev. Mater.* 5 (4) (2020) 295–309. doi:10.1038/s41578-019-0170-8.
- [3] L. Feng, W. G. Fahrenholtz, D. W. Brenner, High-Entropy Ultra-High-Temperature Borides and Carbides: A New Class of Materials for Extreme Environments, *Annu. Rev. Mater. Res.* 51 (1) (2021) 165–185. doi:10.1146/annurev-matsci-080819-121217.
- [4] S. Jiang, T. Hu, J. Gild, N. Zhou, J. Nie, M. Qin, T. Harrington, K. Vecchio, J. Luo, A new class of high-entropy perovskite oxides, *Scripta Mat.* 142 (2018) 116–120. doi:10.1016/j.scriptamat.2017.08.040.
- [5] M. Qin, Q. Yan, Y. Liu, J. Luo, A new class of high-entropy M3B4 borides, *J. Adv. Ceram.* 10 (1) (2021) 166–172. doi:10.1007/s40145-020-0438-x.
- [6] G. N. Kotsonis, S. S. I. Almishal, F. Marques Dos Santos Vieira, V. H. Crespi, I. Dabo, C. M. Rost, J. Maria, High-entropy oxides: Harnessing crystalline disorder for emergent functionality, *J. Am. Ceram. Soc.* 106 (10) (2023) 5587–5611. doi:10.1111/jace.19252.
- [7] N. P. Gurao, K. Biswas, High-Entropy Materials: Critical Review and Way Forward, *Curr. Sci. India* 118 (10) (2020) 1520. doi:10.18520/cs/v118/i10/1520-1539.
- [8] R.-Z. Zhang, M. J. Reece, Review of high entropy ceramics: design, synthesis, structure and properties, *J. Mater. Chem. A* 7 (39) (2019) 22148–22162. doi:10.1039/C9TA05698J.
- [9] Y. Wang, Processing and properties of high entropy carbides, *Adv. Appl. Ceram.* 121 (2) (2022) 57–78. doi:10.1080/17436753.2021.2014277.
- [10] A. Sarkar, R. Djenadic, D. Wang, C. Hein, R. Kautenburger, O. Clemens, H. Hahn, Rare earth and transition metal based entropy stabilised perovskite type oxides, *J. Eur. Ceram. Soc.* 38 (5) (2018) 2318–2327. doi:10.1016/j.jeurceramsoc.2017.12.058.
- [11] M. Qin, Q. Yan, H. Wang, K. S. Vecchio, J. Luo, High-entropy rare earth tetraborides, *J. Eur. Ceram. Soc.* 41 (4) (2021) 2968–2973. doi:10.1016/j.jeurceramsoc.2020.12.019.
- [12] K. Bryce, Y.-T. Shih, L. Huang, J. Lian, Calcium-Magnesium-Aluminosilicate (CMAS) corrosion resistance of high entropy rare-earth phosphate (Lu<sub>0.2</sub>Yb<sub>0.2</sub>Er<sub>0.2</sub>Y<sub>0.2</sub>Gd<sub>0.2</sub>)PO<sub>4</sub>: A novel environmental barrier coating candidate, *J. Eur. Ceram. Soc.* 43 (14) (2023) 6461–6472. doi:10.1016/j.jeurceramsoc.2023.06.030.
- [13] W. Sang, W. Xie, R. Hou, S. Li, H. Zhang, S. Liu, X. Chen, Crystal structure and thermophysical properties of (Gd<sub>0.25</sub>Sm<sub>0.25</sub>Yb<sub>0.25</sub>Y<sub>0.25</sub>)<sub>3</sub>TaO<sub>7</sub> high-entropy oxide, *Ceram. Int.* 49 (17) (2023) 29358–29363. doi:10.1016/j.ceramint.2023.06.151.
- [14] X. Ping, B. Meng, X. Yu, Z. Ma, X. Pan, W. Lin, Structural, mechanical and thermal properties of cubic bixbyite-structured high-entropy oxides, *Chem. Eng. J.* 464 (2023) 142649. doi:10.1016/j.cej.2023.142649.
- [15] Z. Rak, C. M. Rost, M. Lim, P. Sarker, C. Toher, S. Curtarolo, J.-P. Maria, D. W. Brenner, Charge compensation and electrostatic transferability in three entropy-stabilized oxides: Results from density functional theory calculations, *J. Appl. Phys.* 120 (9) (2016) 095105. doi:10.1063/1.4962135.
- [16] J. L. Braun, C. M. Rost, M. Lim, A. Giri, D. H. Olson, G. N. Kotsonis, G. Stan, D. W. Brenner, J.-P. Maria, P. E. Hopkins, Charge-Induced Disorder Controls the Thermal Conductivity of Entropy-Stabilized Oxides, *Adv. Mater.* 30 (51) (2018) 1805004. eprint: <https://onlinelibrary.wiley.com/doi/pdf/10.1002/adma.201805004>. doi:10.1002/adma.201805004.
- [17] M. Lim, Z. Rak, J. L. Braun, C. M. Rost, G. N. Kotsonis, P. E. Hopkins, J.-P. Maria, D. W. Brenner, Influence of mass and charge disorder on the phonon thermal conductivity of entropy stabilized oxides determined by molecular dynamics simulations, *J. Appl. Phys.* 125 (5) (2019) 055105. doi:10.1063/1.5080419.
- [18] M. Lim, D. W. Brenner, Predicting properties of high entropy carbides from their respective binaries, *Comp. Mater. Sci.* 226 (2023) 112255. doi:10.1016/j.commatsci.2023.112255.
- [19] X. Zhao, S. Yu, J. Zheng, M. J. Reece, R.-Z. Zhang, Machine learning of carbon vacancy formation energy in high-entropy carbides, *J. Eur. Ceram. Soc.* 43 (4) (2023) 1315–1321. doi:10.1016/j.jeurceramsoc.2022.11.044.
- [20] V. Vitek, Intrinsic stacking faults in body-centred cubic crystals, *Philos. Mag.* 18 (154) (1968) 773–786. doi:10.1080/14786436808227500.
- [21] N. Bernstein, E. Tadmor, Tight-binding calculations of stacking energies and twinnability in fcc metals, *Phys. Rev. B* 69 (9) (2004) 094116. doi:10.1103/PhysRevB.69.094116.
- [22] E. Tadmor, A first-principles measure for the twinnability of FCC metals, *J. Mech. Phys. Solids* 52 (11) (2004) 2507–2519. doi:10.1016/j.jmps.2004.05.002.
- [23] M. Jahnátek, J. Hafner, M. Krajčí, Shear deformation, ideal strength, and stacking fault formation of fcc metals: A density-functional study of Al and Cu, *Phys. Rev. B* 79 (22) (2009) 224103. doi:10.1103/PhysRevB.79.224103.
- [24] X.-C. Zhang, S. Cao, L.-J. Zhang, R. Yang, Q.-M. Hu, Unstable stacking fault energy and peierls stress for evaluating slip system competition in body-centered cubic metals, *J. Mater. Res. Technol.* 22 (2023) 3413–3422. doi:10.1016/j.jmrt.2022.12.162.
- [25] H. Yu, M. Bahadori, G. B. Thompson, C. R. Weinberger, Understanding dislocation slip in stoichiometric rocksalt transition metal carbides and nitrides, *J. Mater. Sci.* 52 (11) (2017) 6235–6248. doi:10.1007/s10853-017-0857-4.
- [26] C. J. Smith, X.-X. Yu, Q. Guo, C. R. Weinberger, G. B. Thompson, Phase, hardness, and deformation slip behavior in mixed Hf<sub>x</sub>Ta<sub>1-x</sub>C, *Acta Mater.* 145 (2018) 142–153. doi:10.1016/j.actamat.2017.11.038.
- [27] T. Csanádi, V. Girman, Ł. Maj, J. Morgiel, M. J. Reece, J. Dusza, Hardness anisotropy and active slip systems in a (Hf-Ta-Zr-Nb)<sub>3</sub>C high-entropy carbide during nanoindentation, *Int. J. Refract. Met. Hard. Mater.* 100 (2021) 105646. doi:10.1016/j.ijrmhm.2021.105646.
- [28] N. De Leon, X.-x. Yu, H. Yu, C. R. Weinberger, G. B. Thompson, Bonding Effects on the Slip Differences in the B1 Monocarbides, *Phys. Rev. Lett.* 114 (16) (2015) 165502. doi:10.1103/PhysRevLett.114.165502.
- [29] S. L. Shang, W. Y. Wang, Y. Wang, Y. Du, J. X. Zhang, A. D. Patel, Z. K. Liu, Temperature-dependent ideal strength and stacking fault energy of fcc Ni: a first-principles study of shear deformation, *J. Phys.: Condens. Matter* 24 (15) (2012) 155402. doi:10.1088/0953-8984/24/15/155402.
- [30] L. Ma, Z. Wang, J. Huang, G. Huang, M. Xue, P. Tang, T. Fan, Effect of alloying elements on stacking fault energies and twinnabilities in high-entropy transition-metal carbides, *J. Am. Ceram. Soc.* 104 (12) (2021) 6521–6532. doi:10.1111/jace.18025.
- [31] K. Kaufmann, D. Maryanovsky, W. M. Mellor, C. Zhu, A. S. Rosengarten, T. J. Harrington, C. Oses, C. Toher, S. Curtarolo, K. S. Vecchio, Discovery of high-entropy ceramics via machine learning, *npj Comput. Mater.* 6 (1) (2020) 42. doi:10.1038/s41524-020-0317-6.
- [32] P. Sarker, T. Harrington, C. Toher, C. Oses, M. Samiee, J.-P. Maria, D. W. Brenner, K. S. Vecchio, S. Curtarolo, High-entropy high-hardness metal carbides discovered by entropy descriptors, *Nat. Commun.* 9 (1) (2018) 4980. doi:10.1038/s41467-018-07160-7.
- [33] D. Utt, S. Lee, Y. Xing, H. Jeong, A. Stukowski, S. H. Oh, G. Dehm, K. Albe, The origin of jerky dislocation motion in high-entropy alloys, *Nat. Commun.* 13 (1) (2022) 4777. doi:10.1038/s41467-022-32134-1.
- [34] Y. Wang, T. Csanádi, H. Zhang, J. Dusza, M. J. Reece, R. Zhang, En-

- hanced Hardness in High-Entropy Carbides through Atomic Randomness, *Adv. Theory Simul.* 3 (9) (2020) 2000111. doi:10.1002/adts.202000111.
- [35] M. Shih, J. Miao, M. Mills, M. Ghazisaeidi, Stacking fault energy in concentrated alloys, *Nat. Commun.* 12 (1) (2021) 3590. doi:10.1038/s41467-021-23860-z.
- [36] M. G. Evans, M. Polanyi, Inertia and driving force of chemical reactions, *T. Faraday Soc.* 34 (0) (1938) 11–24, publisher: The Royal Society of Chemistry. doi:10.1039/TF9383400011.
- [37] P. E. Blöchl, Projector augmented-wave method, *Phys. Rev. B* 50 (24) (1994) 17953.
- [38] G. Kresse, J. Hafner, Ab initio molecular dynamics for liquid metals, *Phys. Rev. B* 47 (1) (1993) 558.
- [39] G. Kresse, J. Furthmüller, Efficiency of ab-initio total energy calculations for metals and semiconductors using a plane-wave basis set, *Comput. Mater. Sci.* 6 (1) (1996) 15–50.
- [40] G. Kresse, J. Furthmüller, Efficient iterative schemes for ab initio total-energy calculations using a plane-wave basis set, *Phys. Rev. B* 54 (16) (1996) 11169.
- [41] J. P. Perdew, K. Burke, M. Ernzerhof, Generalized gradient approximation made simple, *Phys. Rev. Lett.* 77 (18) (1996) 3865.
- [42] H. Ding, X. Fan, K. Chu, X. Zhang, X. Liu, The influence of carbon vacancies on the stacking fault energy of TiC, *J. Eur. Ceram. Soc.* 34 (7) (2014) 1893–1897. doi:10.1016/j.jeurceramsoc.2014.01.013.
- [43] S. E. Daigle, D. W. Brenner, Statistical approach to obtaining vacancy formation energies in high-entropy crystals from first principles calculations: Application to a high-entropy diboride, *Phys. Rev. Mater.* 4 (12) (2020) 123602. doi:10.1103/PhysRevMaterials.4.123602.
- [44] Q. Meng, X. Lin, Y. Zhai, L. Zhang, P. Zhang, L. Sheng, A theoretical investigation on Bell-Evans-Polanyi correlations for hydrogen abstraction reactions of large biodiesel molecules by H and OH radicals, *Combust. Flame* 214 (2020) 394–406. doi:10.1016/j.combustflame.2020.01.005.
- [45] P. Pla, Y. Wang, M. Alcamí, When is the Bell–Evans–Polanyi principle fulfilled in Diels–Alder reactions of fullerenes?, *Phys. Chem. Chem. Phys.* 22 (16) (2020) 8846–8852. doi:10.1039/C9CP06977A.
- [46] G. G. Wubbels, The Bell–Evans–Polanyi Principle and the regioselectivity of electrophilic aromatic substitution reactions, *Tetrahedron Lett.* 56 (13) (2015) 1716–1719. doi:10.1016/j.tetlet.2015.02.070.
- [47] Y. Chen, K. Chang, F. Meng, S. Tseng, P. Chou, Broadening the Horizon of the Bell–Evans–Polanyi Principle towards Optically Triggered Structure Planarization, *Angew. Chem. Int. Ed.* 60 (13) (2021) 7205–7212. doi:10.1002/anie.202015274.
- [48] Z.-Y. Liu, Y.-C. Wei, P.-T. Chou, Correlation between Kinetics and Thermodynamics for Excited-State Intramolecular Proton Transfer Reactions, *J. Phys. Chem. A* 125 (30) (2021) 6611–6620. doi:10.1021/acs.jpca.1c04192.
- [49] E. F. Sheka, Virtual Free-Radical Polymerization of Vinyl Monomers in View of Digital Twins, *Polymers* 15 (14) (2023) 2999. doi:10.3390/polym15142999.
- [50] R. T. Garrod, M. Jin, K. A. Matis, D. Jones, E. R. Willis, E. Herbst, Formation of Complex Organic Molecules in Hot Molecular Cores through Nondiffusive Grain-surface and Ice-mantle Chemistry, *Astrophys. J. Suppl. Ser.* 259 (1) (2022) 1. doi:10.3847/1538-4365/ac3131.
- [51] J. Cheng, P. Hu, P. Ellis, S. French, G. Kelly, C. M. Lok, Brønsted-Evans-Polanyi Relation of Multistep Reactions and Volcano Curve in Heterogeneous Catalysis, *J. Phys. Chem. C* 112 (5) (2008) 1308–1311. doi:10.1021/jp711191j.
- [52] R. G. Agarwal, J. M. Mayer, Coverage-Dependent Rate-Driving Force Relationships: Hydrogen Transfer from Cerium Oxide Nanoparticle Colloids, *J. Am. Chem. Soc.* 144 (45) (2022) 20699–20709. doi:10.1021/jacs.2c07988.
- [53] B. Pascucci, G. Otero, P. Belelli, M. Branda, Understanding the effects of metal particle size on the NO<sub>2</sub> reduction from a DFT study, *Apple. Surf. Sci.* 489 (2019) 1019–1029. doi:10.1016/j.apsusc.2019.05.318.
- [54] T. Kropp, M. Mavrikakis, Brønsted–Evans–Polanyi relation for CO oxidation on metal oxides following the Mars–van Krevelen mechanism, *J. Catal.* 377 (2019) 577–581. doi:10.1016/j.jcat.2019.08.002.
- [55] H. Jia, Z. Kang, S. Li, Y. Li, J. Ge, D. Feng, Thermal degradation behavior of seawater based temporary plugging gel crosslinked by polyethyleneimine for fluid loss control in gas well: Kinetics study and degradation prediction, *J. Disper. Sci. Technol.* 42 (9) (2021) 1299–1310. doi:10.1080/01932691.2020.1740727.
- [56] M. K. Phuthi, A. M. Yao, S. Batzner, A. Musaelian, B. Kozinsky, E. D. Cubuk, V. Viswanathan, Accurate Surface and Finite Temperature Bulk Properties of Lithium Metal at Large Scales using Machine Learning Interaction Potentials (preprint; 2023). doi:10.48550/arXiv.2305.06925.
- [57] S. Zeman, Modified Evans–Polanyi–Semenov relationship in the study of chemical micromechanism governing detonation initiation of individual energetic materials, *Thermochim. Acta* 384 (1-2) (2002) 137–154. doi:10.1016/S0040-6031(01)00787-0.
- [58] G. Luo, X. Wang, M. R. Zachariah, R. Mishra, Ignition Threshold of Perovskite-Based Oxides for Solid Fuel Oxidation from First-Principles Calculations, *J. Phys. Chem. C* 123 (29) (2019) 17644–17649. doi:10.1021/acs.jpcc.9b01609.
- [59] M. J. Cawkwell, J. Davis, N. Lease, F. W. Marrs, A. Burch, S. Ferreira, V. W. Manner, Understanding Explosive Sensitivity with Effective Trigger Linkage Kinetics, *ACS Phys. Chem. Au* 2 (5) (2022) 448–458. doi:10.1021/acsphyschemau.2c00022.
- [60] E. Zurek, Discovering New Materials via A Priori Crystal Structure Prediction, in: *Reviews in Computational Chemistry*, John Wiley & Sons, Ltd, 2016, pp. 274–326. doi:10.1002/9781119148739.ch5.
- [61] C. Barrales-Martínez, P. Jaque, A deeper analysis of the role of synchronicity on the Bell–Evans–Polanyi plot in multibond chemical reactions: a path-dependent reaction force constant, *Phys. Chem. Chem. Phys.* 24 (24) (2022) 14772–14779. doi:10.1039/D2CP01460B.
- [62] S. Roy, S. Goedecker, V. Hellmann, Bell-Evans-Polanyi principle for molecular dynamics trajectories and its implications for global optimization, *Phys. Rev. E* 77 (5) (2008) 056707. doi:10.1103/PhysRevE.77.056707.
- [63] A. F. Shestakov, Quantum-Chemical Verification of the Polanyi–Semenov Generalized Relationship, *Dokl. Phys. Chem.* 393 (4-6) (2003) 339–342. doi:10.1023/B:D0PC.0000010338.43734.4a.
- [64] S.-H. Jhi, J. Ihm, S. G. Louie, M. L. Cohen, Electronic mechanism of hardness enhancement in transition-metal carbonitrides, *Nature* 399 (6732) (1999) 132–134. doi:10.1038/20148.
- [65] K. Balasubramanian, S. V. Khare, D. Gall, Valence electron concentration as an indicator for mechanical properties in rocksalt structure nitrides, carbides and carbonitrides, *Acta Mater.* 152 (2018) 175–185. doi:10.1016/j.actamat.2018.04.033.
- [66] E. T. Denisov, New empirical models of radical abstraction reactions, *Russ. Chem. Rev.* 66 (10) (1997) 859–876. doi:10.1070/RC1997v066n10ABEH000364.
- [67] Z. Pei, S. Zhang, Y. Lei, F. Zhang, M. Chen, Decoupling between Shockley partials and stacking faults strengthens multiprincipal element alloys, *Proc. Natl. Acad. Sci. U.S.A.* 118 (51) (2021) e2114167118. doi:10.1073/pnas.2114167118.
- [68] S.-Y. Liu, S. Zhang, S. Liu, D.-J. Li, Z. Niu, Y. Li, S. Wang, Stability and mechanical properties of single-phase quinary high-entropy metal carbides: First-principles theory and thermodynamics, *J. Eur. Ceram. Soc.* 42 (7) (2022) 3089–3098. doi:10.1016/j.jeurceramsoc.2022.02.034.
- [69] C. Nam, Prediction of mechanical properties of high-entropy ceramics by deep learning with compositional descriptors, *Mater. Today Commun.* 35 (2023) 105949. doi:10.1016/j.mtcomm.2023.105949.